



Cite this: *Phys. Chem. Chem. Phys.*,
2016, **18**, 22146

A facile synthesis of three dimensional graphene sponge composited with sulfur nanoparticles for flexible Li–S cathodes†

Chao Lin,^{‡a} Chaojiang Niu,^{‡a} Xu Xu,^a Ke Li,^b Zhengyang Cai,^a Yonglai Zhang,^b Xuanpeng Wang,^a Longbing Qu,^a Yuxi Xu^{*b} and Liqiang Mai^{*a}

Compared with a two dimensional graphene sheet, a three dimensional (3D) graphene sponge has a continuous conductive structure and numerous pores, which are beneficial for sulfur utilization and anchoring. However, strategies for the construction of 3D graphene sponges composited with sulfur nanoparticles (3DGS) are either energy consuming or involve toxic reagents. Herein, a 3DGS is fabricated via a reduction induced self-assembly method, which is simple but facile and scalable. The structural design of this 3DGS promises fast Li⁺ transport, superior electrolyte absorbability and effective electrochemical redox reactions of sulfur. As a result, this 3DGS achieves a stable capacity of 580 mA h g⁻¹ after 500 cycles at a high rate of 1.5 A g⁻¹, which corresponds to a low fading rate of 0.043% per cycle. The present study effectively demonstrates that the 3D construction strategy is propitious for obtaining flexible high performance Li–S batteries.

Received 26th May 2016,
Accepted 5th July 2016

DOI: 10.1039/c6cp03624d

www.rsc.org/pccp

Introduction

The ever-increasing demand for high capacity energy storage systems has stimulated intense scrutiny over new secondary batteries.^{1–5} Li–S batteries, with a safe operating voltage (2.15 V vs. Li⁺/Li),⁶ have been regarded as one of the potential candidates owing to their high theoretical specific capacity (1675 mA h g⁻¹) and energy density (2600 W h kg⁻¹).^{4,7–9} Besides, as the raw material for Li–S batteries, sulfur is cheap, abundant in the earth's crust and environmentally friendly. Nevertheless, several major challenges regarding Li–S batteries have limited their widespread practical application. For example, the intrinsic insulating nature of sulfur and its reduced products have an unfavourable influence on the effectual utilization of the active material and the rate performance of the battery. In addition, the highly soluble intermediate lithium polysulfides could migrate between the electrodes during cycling and form solid precipitates (*i.e.*, Li₂S and Li₂S₂) on the surface of the electrodes, resulting in low coulombic efficiency due to an internal redox shuttle. Moreover, the large volume variation (*ca.* 80%) caused by the transformation between sulfur

and Li₂S during cycling processes de-escalates the mechanical integrity of the electrode, which ultimately leads to poor cell reversibility.^{10–14}

To address these challenges, numerous strategies have been explored, including the improvement of the electrolyte,^{15–18} designing new structural polymer/sulfur composites^{19–21} or carbon/sulfur composites,²² modifying the electrodes with metal oxides^{23–26} and optimizing the cell configuration.^{27–30} It is noted that carbonaceous matrices, such as carbon nanotubes/nanofibers,^{31–34} porous carbon,^{35,36} hollow carbon spheres^{9,37} and graphene,^{6,38,39} could not only enhance the electrical conductivity, but also alleviate the dissolution of polysulfides through physical adsorption. Among them, reduced graphene oxide (rGO) has been successfully applied in Li–S cathodes owing to its superior conductivity and excellent mechanical flexibility. It has been demonstrated that the rich functional groups on rGO have strong chemical interactions with the polysulfide ions,^{22,40} hence suppressing the shuttle effect. However, the rGO fails to trap the polysulfides over long-term cycling due to its open structure. Fortunately, the construction of a porous and interconnected three dimensional (3D) graphene sponge helps to offset the inferiority of rGO in the practical application of Li–S batteries.

Up till now, various methods for the construction of 3D graphene/sulfur composite have been proposed. For example, Hu *et al.*⁴¹ adopted a chemical vapour deposition method to fabricate a highly conductive graphene framework nested with rGO aerogel, which was followed by a melt-diffusion process at 155 °C. Zhou *et al.*²² reported a one-pot strategy using a

^a State Key Laboratory of Advanced Technology for Materials Synthesis and Processing, Wuhan University of Technology, Wuhan 430070, China. E-mail: mlq518@whut.edu.cn

^b State Key Laboratory of Molecular Engineering of Polymers, Department of Macromolecular Science, Fudan University, Shanghai 200433, China. E-mail: xuyuxi@fudan.edu.cn

† Electronic supplementary information (ESI) available: Calculations of sulfur content and the electrolyte uptake ability, Fig. S1–S8. See DOI: 10.1039/c6cp03624d
‡ These authors contributed equally to this work.

sulfur/carbon disulfur (CS₂)/alcohol mixed solution. Despite this progress, the methods involved are either energy consuming^{42–45} or use toxic CS₂ to dissolve the sulfur.^{22,46} In most cases, auxiliary materials such as polymeric binder and conductive additives are indispensable when the synthesized 3D graphene/sulfur composites are used as electrodes.^{47–50} These materials reduce the overall energy density of the electrode and sacrifice part of the active material during long-term cycling.⁵¹ Therefore, the facile construction of a 3D graphene sponge for binder-free Li–S cathodes is necessary.

Herein, we adopt a facile and environmentally-benign approach to fabricate a 3D graphene sponge with sulfur particles uniformly anchored through a one-pot reduction induced self-assembly process. This approach can be easily scaled up due to the simple but facile fabrication process. The 3D construction has multiple advantages. Specifically, the interconnected porous conductive framework provides continuous electronic conductivity and facilitates the penetration of the electrolyte, reducing the resistance towards electron and ion transport during the cycling process. Additionally, the residual functional groups on the rGO offer numerous adhesion points for the polysulfides and the pores ensure superior electrolyte absorbability, thus alleviating the shuttle effect. The electrode manifests robust structural integrity and outstanding flexibility, showing great potential as a flexible cathode for Li–S batteries.

Experimental

All chemicals were purchased from Aladdin or Sigma Aldrich and used as received without further purification. Graphene oxide (GO) was prepared *via* a modified Hummers' method.⁵²

Synthesis of 3D graphene sponge composited with sulfur nanoparticles (3DGS)

6.7 g Na₂S₂O₃·5H₂O was dissolved in 1.4 L of a GO aqueous suspension (0.3 mg mL⁻¹) and stirred for 10 min at 0 °C. 0.5 L diluted HCl aqueous solution (0.024 M) was added dropwise to the above solution under magnetic stirring. The reaction proceeded overnight. The final product was collected and was washed with deionized water. The obtained product was re-dispersed into 280 mL deionized water to form a precursor. 0.75 mL of a sodium ascorbate (C₆H₇O₆Na) aqueous solution (1 M) was mixed ultrasonically with 20 mL precursor and heated at 95 °C for 1.5 h. The as-prepared 3DGS hydrogels were taken out and immersed in deionized water to remove any impurities, followed by freeze-drying to obtain the 3DGS sponge.

Synthesis of sulfur-reduced graphene oxide composite (GS)

4.17 mL C₆H₇O₆Na aqueous solution (1 M) was added to 110 mL (1.5 mg mL⁻¹) GO aqueous suspension, which was followed by magnetic stirring for 1.5 h at 95 °C. The synthesized reduced graphene oxide was collected and washed by vacuum filtration and then re-dispersed into 400 mL of pure water. 2.6 g Na₂S₂O₃·5H₂O was added to the above dispersion with magnetic stirring for 10 min at 0 °C. After that, 200 mL diluted HCl aqueous solution (0.024 M) was added slowly. The reaction proceeded overnight

before the product was filtered, washed with deionized water, and freeze-dried.

Characterization

The morphology observations were performed on a field emission scanning electron microscope (FESEM, Zeiss, Ultra 55) and a transmission electron microscope (TEM, Tecnai G2 20 TWIN). Energy dispersive spectra (EDS) were used for elemental analysis. X-ray diffraction (XRD) measurements were conducted by an X'pert PRO XRD equipped with Cu K α radiation from 10° to 80° at a scan rate of 0.04° s⁻¹. Fourier Transform Infrared (FTIR) spectra were recorded for chemical bonding analysis. Raman spectroscopy experiments were carried out with He–Ne laser excitation at 538 nm using a Horiba Jobin Yvon LabRAM HR800 Raman spectrometer. The thermogravimetric analysis (TGA) data were collected with a Pyris1 Thermogravimetric Analyzer at a heating rate of 10 °C min⁻¹ under a nitrogen atmosphere. The Brunauer–Emmett–Teller surface area was measured using a Gemini 2360 instrument by the adsorption of nitrogen at –197 °C. X-Ray photoelectron spectra (XPS) data were collected with a RBD upgraded PHI-5000C ESCA system (Perkin Elmer) with Mg K α radiation ($h\nu = 1253.6$ eV).

Electrochemical characterization

The 3DGS was compressed and cut into circular disks which could be used directly as an electrode. A GS cathode was prepared by mixing the active material, acetylene black and polyvinylidene fluoride (PVDF) binder in a mass ratio of 7:2:1 in *N*-methyl pyrrolidinone (NMP) to form a homogeneous slurry. The slurry was spread onto aluminum foils with a 100 μ m doctor blade and dried at 50 °C in a vacuum oven for 12 h. The dried foil sheet was pressed and cut into a circular disk with a diameter of 15 mm which served as a cathode. The areal mass loading of sulfur was ~ 2 mg cm⁻². The electrochemical performance was evaluated using coin cells with lithium metal as the counter and reference electrode and a Celgard 2400 membrane as the separator. The electrolyte solution was 1.0 M LiTFSI in a solvent of DOL:DME (1:1 in volume) with an additive of 0.1 M LiNO₃. Galvanostatic measurements were conducted using a LAND CT2001A battery test system between 1.7 and 2.8 V (*vs.* Li⁺/Li). The specific capacity was calculated based on the mass of sulfur. Cyclic voltammogram (CV) experiments and electrochemical impedance spectroscopy (EIS) measurements were conducted using a CHI 760E electrochemical workstation. The CVs were recorded at a scan rate of 0.1 mV s⁻¹ within a cutoff window of 1.6–2.8 V. The EIS was measured by applying a disturbance amplitude of 5 mV in a frequency range of 10⁻²–10⁵ Hz.

Results and discussion

The overall synthetic procedure of the 3DGS electrode is illustrated in Fig. 1a. Typically, the 3DGS precursor was first fabricated from the *in situ* growth of sulfur nanoparticles on graphene oxide by dropping HCl solution slowly into the homogenous suspension of GO and sodium thiosulfate. Finally, the 3DGS sponge was obtained

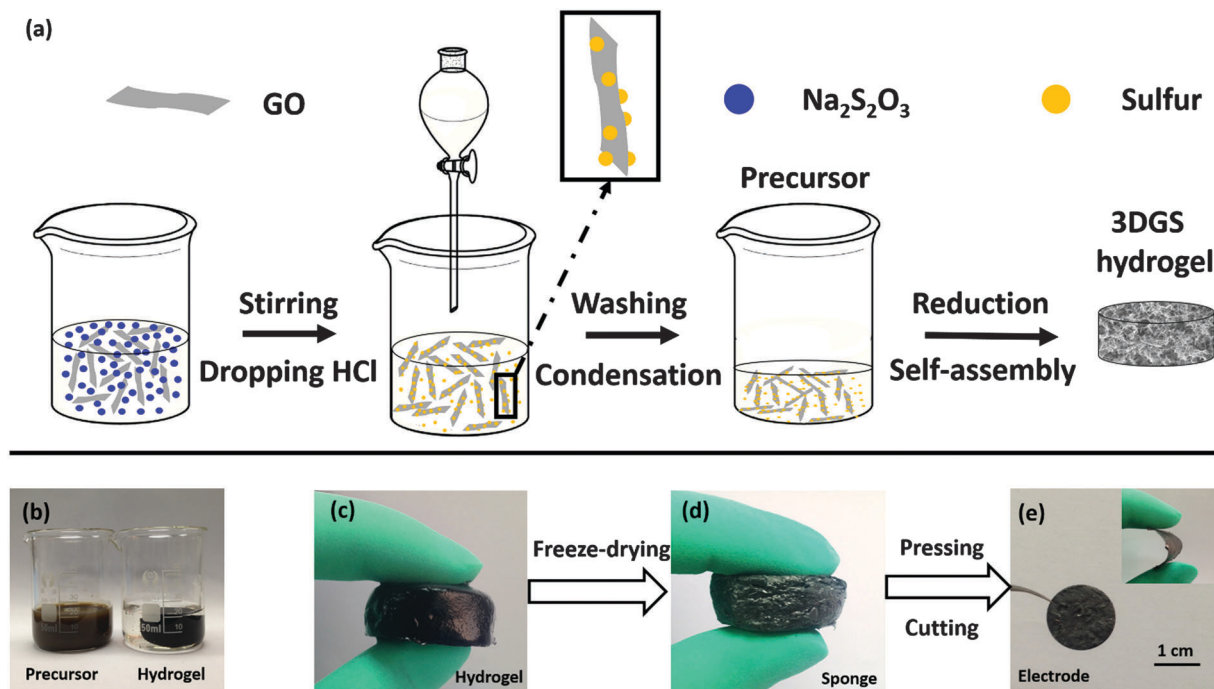


Fig. 1 (a) Schematic illustration of the fabrication process of the 3DGS cathode; digital images of (b) the precursor before and after reduction-induced self-assembly, (c) hydrogel, (d) sponge, (e) electrode.

through the reduction induced self-assembly⁵² and freeze-drying. Such a process can be easily scaled up due to the facile synthesis conditions. In our laboratory, the yield of one pot is about 3 grams for one batch of precursor (Fig. S1 of ESI[†]), and the maximum amount of 3DGS produced from one 5 L beaker at one time is about 2.2 grams due to the limited lab conditions. The precursor can be readily transformed into the mechanically strong monolithic 3DGS hydrogel with few sulfur particles left in the solution (Fig. 1b), indicating that rGO and sulfur are conjugated together. Both the 3DGS hydrogel (Fig. 1c) and sponge (Fig. 1d) exhibit a robust and free-standing structure. The 3DGS electrode has a diameter of

15 mm (Fig. 1e) and exhibits outstanding integrity and superior flexibility (inset of Fig. 1e).

The morphologies and the microstructures of the 3DGS and GS were investigated by SEM and TEM, respectively. The as-prepared 3DGS samples maintain intrinsic interlinked porous networks with pore sizes ranging from submicrometers to several micrometers. In addition, no obvious bare sulfur was observed (Fig. 2a and b). Even after being compressed, the interconnected porous structure still exists (Fig. S2 of ESI[†]), which is beneficial for ion transport and it could accommodate the volume variation of sulfur during cycling. The thickness of the compressed 3DGS is about 100 μm

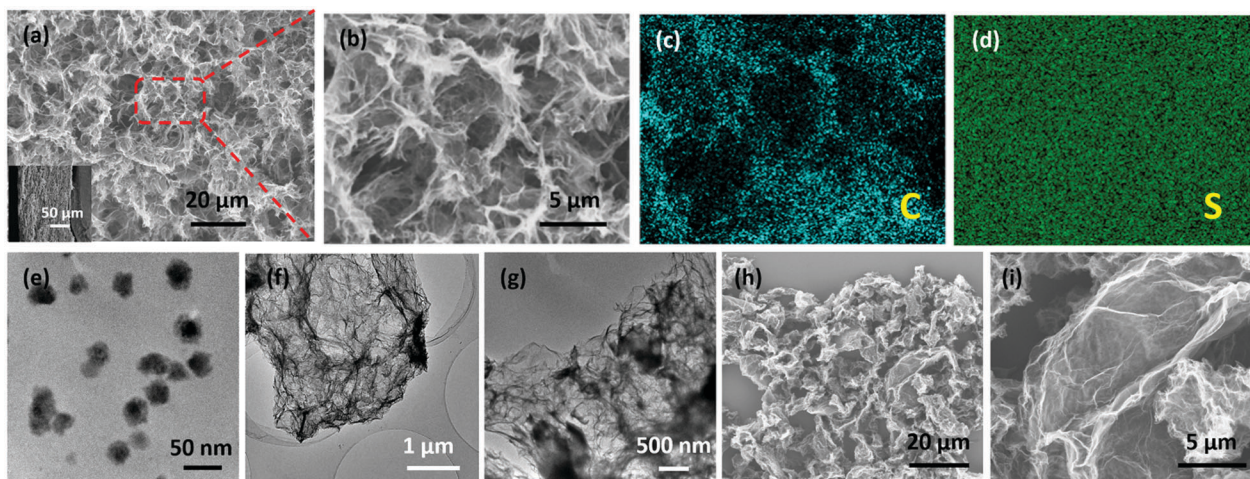


Fig. 2 SEM images of 3DGS sponge (a and b), and corresponding elemental mapping images of carbon (c) and sulfur (d); TEM images of 3DGS precursor (e), 3DGS (f and g); SEM images of GS (h and i), the inset of (a) is a cross sectional SEM image of the 3DGS electrode.

(inset of Fig. 2a) and the control sample has the same thickness value. The sulfur in 3DGS may be distributed homogeneously over the whole graphene sponge, deduced from its homogeneous distribution on the front (Fig. 2b–d) and in a cross-section (Fig. S3 of ESI†) of 3DGS. Moreover, the sulfur shows a more uniform distribution than graphene (Fig. 2b–d, Fig. S3 of ESI†), indicating that the sulfur was not only anchored on the graphene nanosheet, but also filled the pores of the graphene sponge. The TEM image (Fig. 2f) also reveals the porous structure of 3DGS, which is consistent with the result of the SEM images. No significant fraction of bulk sulfur is exposed on the graphene sponge (Fig. 2g). This may result from the sublimation of sulfur under the high voltage and vacuum of TEM.³⁷ However, there are nano-sized sulfur particles with a diameter of about 20 nm in the 3DGS precursor (Fig. 2e), indicating strong bonding between the functional groups and the sulfur particles.⁵³ In contrast, GS composites (Fig. 2h and i) exhibit isolated layer-like conjugated nanostructures with no naked sulfur particles observed either.

The structural characteristics of GS and 3DGS were determined by X-ray diffraction (XRD), as shown in Fig. 3a. In comparison with the GS, the characteristic peaks of *Fddd* orthorhombic sulfur (JCPDS NO. 08-0247) of 3DGS composites become much weaker, indicating that the sulfur of 3DGS exists in a low crystallization state. The difference between GS and 3DGS in the XRD patterns demonstrates that the graphene oxide solution may have an effect in facilitating the heterogeneous nucleation of sulfur on the graphene oxide nanosheet surface due to it being rich in functional groups, and achieving slow interfacial growth of low crystalline sulfur nanoparticles,^{6,50} as evidenced by the TEM image (Fig. 2e). Obviously, the peaks at 23.6° of GS and 3DGS composites reveal the reduced intensity of GO in the composites. The Raman spectra of GS and 3DGS are given in Fig. 3b. Two strong peaks located at about 1590 and 1350 cm⁻¹ are attributed to the G (ordered) and D

(disordered) bands of graphene,³⁸ respectively. The same intensity ratio of the D band and the G band (I_D/I_G) is ascribed to there being the same degree of graphitization intensity in both 3DGS and GS. To verify the effective reduction of GO in both composites, FTIR spectra were further collected (Fig. 3c). Compared with GO, three peaks at 1732, 1623 and 1053 cm⁻¹, which are ascribed to C=O bonds, carboxyl O=C-O and C-O bonds^{48,49} in both the 3DGS and GS composites, are greatly weakened, indicating that the GO has been reduced to rGO. Interestingly, a new peak at 1543 cm⁻¹ appears in the spectra of 3DGS and GS, which is attributed to the stretching vibrations of S=O.⁴⁸ The S=O bonds could help with immobilizing the polysulfides during cycling. The sulfur contents of 3DGS and GS were measured using TGA (Fig. S4a of ESI†). The main weight loss of rGO, 3DGS and GS at the temperature range from 150 °C to 500 °C was 11.6 wt%, 59.7 wt% and 76.5 wt%, respectively, demonstrating that the S content in the 3DGS and GS composites were 54.4 wt% and 73.4 wt%, respectively (the calculation process is shown in the ESI†). To make the comparison convective, we made the GS slurry at a ratio of 7 : 2 : 1 (composite : conductive additive : binder). In this way, taking the binder and conductive additive into account, the sulfur content of GS electrode (51.4 wt%) was nearly the same as that of the 3DGS electrode (54.4 wt%).

To elucidate the interaction between rGO and sulfur, X-ray photoelectron spectroscopy (XPS) measurements were carried out on 3DGS directly without any further treatment. The full XPS spectrum of 3DGS contains three peaks related to S, C and O elements that are marked in Fig. S4b of the ESI.† The C 1s signal of 3DGS (Fig. 3d) is composed of four component peaks centered at 284.4, 285.7, 287.0 and 289.1 eV.⁴⁸ The main peak at 284.4 eV is assigned to C-C/C=C. The peaks with higher binding energies at 285.7, 287.0 and 289.1 eV correspond to C-O/C-S, C=O and O-C=O, respectively. These reveal that the

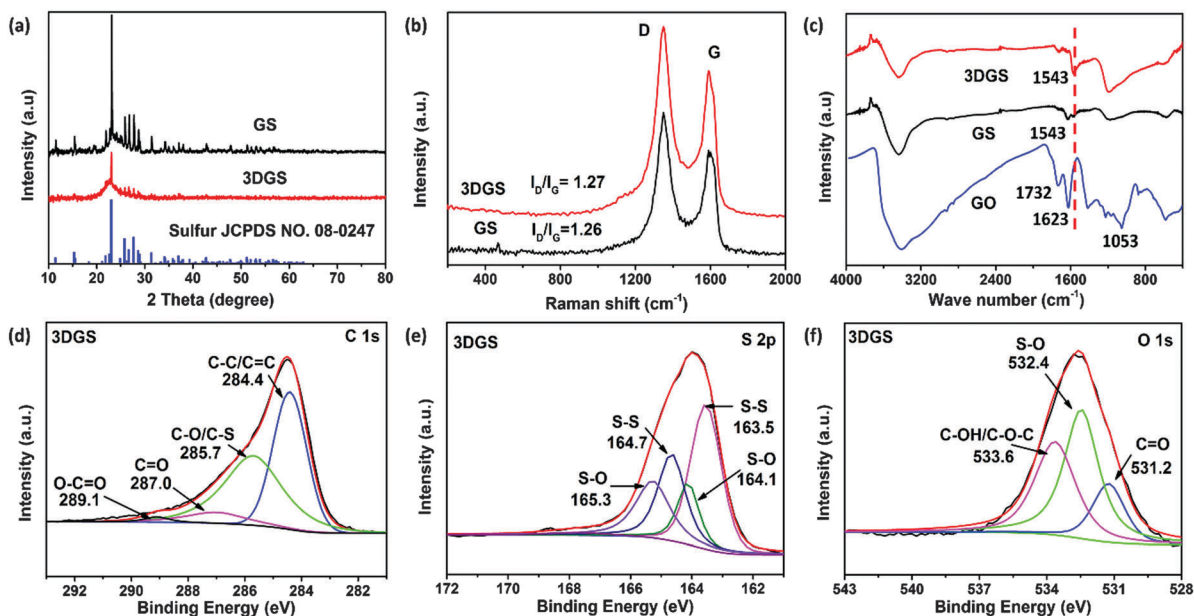


Fig. 3 (a) XRD patterns of 3DGS and GS; (b) Raman spectra of 3DGS and GS; (c) FT-IR spectra of 3DGS, GS and GO; (d–f) XPS spectra of 3DGS: (d) C 1s, (e) S 2p, (f) O 1s.

sulfur nanoparticles could be chemically bonded to the rGO in the 3DGS composite. In the S 2p spectrum of 3DGS (Fig. 3e), the S 2p_{3/2} (163.5 and 164.7 eV) and S 2p_{1/2} (164.1 and 165.3 eV) peaks, with an energy separation of 1.2 eV, are ascribed to the S–S bonds and S–O bonds.⁵⁴ The O 1s spectrum of 3DGS can be resolved into three peaks (Fig. 3f). The peak at 531.2 eV is attributed to C=O groups, while the peak at 533.6 eV is attributed to C–OH and/or C–O–C groups. The peak centered at 532.4 eV is ascribed to the formation of S–O bonds.⁸ These results are in good agreement with the S 2p results, suggesting that sulfur nanoparticles keep an intimate contact with graphene through S–O bonding, and the S–O bonding could effectively immobilize sulfur and restrain the corresponding polysulfides during cycling, thus suppressing the shuttle effect and enhancing the cyclability.^{8,22,48}

The pore size and surface area of 3DGS (Fig. S5 of ESI†) were evaluated using pore size distribution analysis and N₂ adsorption/desorption isotherms. The pore size of 3DGS falls mainly in the range of 1–10 nm. Compared with the results of a graphene sponge synthesised in our previous work,⁵⁵ the BET surface area decreases sharply (from 260 to 20 m² g⁻¹), which is ascribed to the sulfur being loaded into the inner pores of the graphene sponge.

The electrochemical behaviours of the 3DGS and GS composites were characterized by assembling coin cells (2016 type). The CV curves (Fig. 4a) were collected to study the reaction mechanism of the 3DGS electrode. In the first cathodic scan, two pronounced reduction peaks at 2.35 and 2.03 V correspond to a multistep reduction process of sulfur.^{25,50} The first step is attributed to the conversion of S₈ to long-chain polysulfides (Li₂S_n, 4 ≤ n ≤ 8). The second is ascribed to the further reduction of long-chain polysulfides to insoluble Li₂S. In the corresponding anodic scan, the oxidation peaks stabilize at

2.36 and 2.43 V, suggesting a two plateau oxidation process of Li₂S into polysulfides and eventually to elemental sulfur.³⁹ Notably, the CV profiles overlap well in the subsequent cycles, indicating a relatively stable cyclic performance.

The effect of the 3D structure on the rate capability of the 3DGS composite was studied in the galvanostatic mode at discharge–charge current densities from 0.1 to 2 A g⁻¹ (Fig. 4b). As the current densities increase, specific capacities of 1480, 1280, 1100, 880 and 660 mA h g⁻¹ are obtained at 0.1, 0.2, 0.5, 1 and 2 A g⁻¹, respectively. In contrast, this rate performance is overwhelmingly better than that of the GS electrode which was prepared *via* a common traditional method. Importantly, when the current density returns to 0.1 A g⁻¹, a relatively high reversible capacity of 1290 mA h g⁻¹ is attained, suggesting a good reversibility of 3DGS. The corresponding charge and discharge profiles of the 3DGS electrode (Fig. 4c) at various current densities show two voltage plateaus at 2.3–2.4 V and 1.9–2.1 V in the discharge profile, which are consistent with the CV results.⁴⁸ Moreover, the charge and discharge plateaus of this 3DGS electrode change very little with the increase in current densities, indicating low polarization during the charge and discharge processes.

The long-term cycling stability of 3DGS and GS was investigated to clarify the effects of the well-designed 3D structure with nano-sized sulfur anchored within. After the initial two cycles at 100 mA g⁻¹, 3DGS and GS electrodes were then continually cycled at a current density of 1.5 A g⁻¹ (Fig. 4d). Compared with the GS electrode, the 3DGS electrode shows a relatively high specific capacity of 740 mA h g⁻¹ (410 mA h g⁻¹ for GS electrode), indicating the greater utilization of sulfur in the highly porous and conductive graphene framework. Particularly, the 3DGS cathode can operate stably for as long as 500 cycles. The 500th discharge capacity is 580 mA h g⁻¹, corresponding to a high

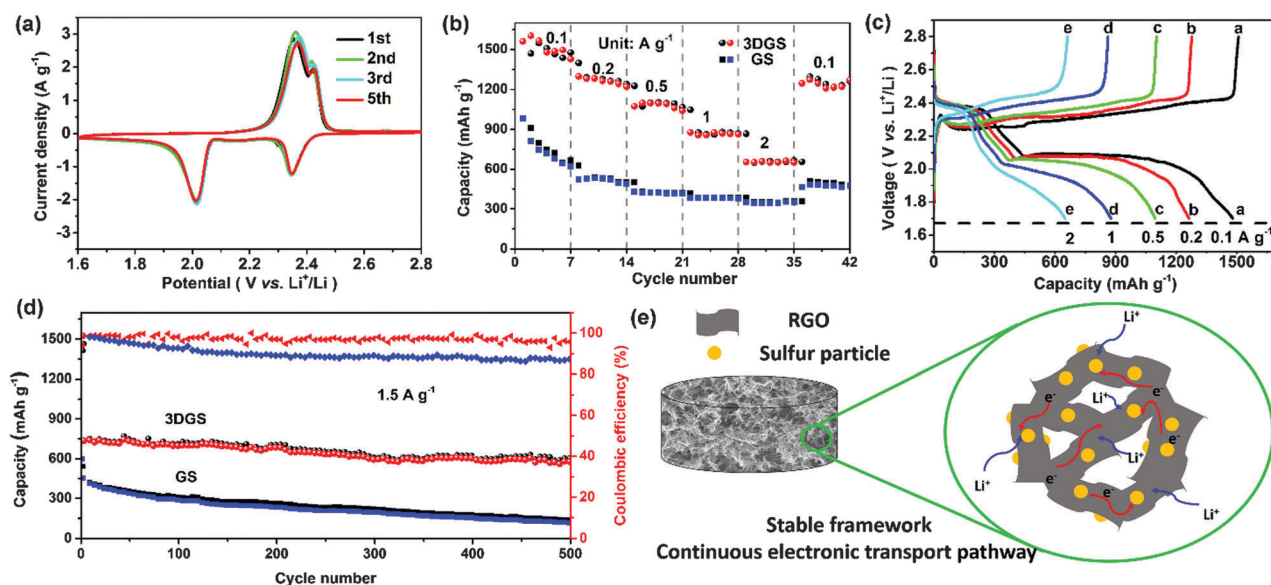


Fig. 4 (a) CV curves of 3DGS at the scan rate of 0.1 mV s⁻¹; (b) rate capability of 3DGS and GS at various current densities from 0.1 to 2 A g⁻¹; (c) charge and discharge profiles of 3DGS at different current densities from 0.1 to 2 A g⁻¹; (d) cyclic performance of the 3DGS and GS cathodes at 1.5 A g⁻¹ for 500 cycles and the corresponding coulombic efficiency; (e) schematic illustration of the 3DGS composite with a continuous electronic transport pathway and stable framework.

capacity retention of 78.4% and to a low decay rate of 0.043% per cycle. This cycling performance is comparable with 3D graphene and sulfur composites that have similar sulfur mass loadings, whether the electrodes are complicatedly fabricated with or without conductive additive and binder (Table S1 of ESI†). Moreover, an impressive energy density of about 600 kW h kg⁻¹ can be calculated based on the whole electrode, even though the sulfur content is low. This energy density is comparable with common lithium ion battery materials, such as LiCoO₂ and LiFePO₄ whose theoretical energy densities are about 532 kW h kg⁻¹ and 578 kW h kg⁻¹ (calculated based on the active materials),⁵⁶ respectively. However, the capacity retention of the GS electrode is only 29.3% after 500 cycles. The cycling stability of the 3DGS electrode is much better than that of the GS electrode, indicating that the interconnected 3D structure is favourable towards the cycling stability. A similar result is attained at a lower current density. The 3DGS electrode still maintains a reversible capacity of 590 mA h g⁻¹ after 500 cycles at 1 A g⁻¹, corresponding to a capacity retention of 66.3% (Fig. S6a of ESI†), while the GS electrode only maintains a reversible capacity of 120 mA h g⁻¹ with a capacity retention of 29.3%. After cycling at a high current density of 2 A g⁻¹ for 300 cycles (Fig. S6b of ESI†), the 3DGS electrode still retains a discharge capacity of 580 mA h g⁻¹, corresponding to a capacity retention of 77.1% and to a low fading rate of 0.076% per cycle. Besides, the cycling performance of the 3DGS electrode at high current density is more stable, which is mainly ascribed to the less severe shuttle effects due to the fast charge and discharge processes.⁵⁷ The coulombic efficiencies of both electrodes fall over long-term cycling (Fig. 4d), which is ascribed to the inevitable shuttle effect (Fig. S7 of ESI†) and the consumption of LiNO₃.^{8,38} However, the coulombic efficiency of 3DGS maintains higher values than those for the GS electrode, suggesting that the shuttle effect is inhibited to some extent.

To understand the electrochemical performance of the 3DGS and GS electrode, electrochemical impedance measurements were also conducted to evaluate the electrochemical kinetics (Fig. S8 of ESI†). Before cycling, the 3DGS cathode exhibits a smaller semicircle, indicating a lower charge transfer resistance (57.17 Ω) compared to that of the GS cathode (73.11 Ω), which can be attributed to the better conductivity of the 3DGS electrode due to its interconnected porous structure. After hundreds of cycles, it is obvious that the resistance of the two electrodes decreases, which is ascribed to the dissolution and redistribution of the active material. The 3DGS cathode still reveals a smaller semicircle under the high and middle frequency regions compared to the GS cathode, indicating faster reaction kinetics and the more uniform deposition of the insulating Li₂S. To confirm our assumption, we disassembled the coin cell after long-term cycling to check the morphology change of the 3DGS electrode. Even after 500 cycles, the electrode still maintains the same structure and no cracks appeared (Fig. S9 of ESI†). There are some deposits inside the continuous interconnected graphene sponge, but no bulk agglomerates of the discharged products are observed on the surface. This phenomenon demonstrates that the flexible 3DGS could relax

the stress arising from the deformation of sulfur and effectively confine the polysulfides by absorbing the electrolyte^{41,58} and the interaction between polysulfide ions and the functional groups²² on graphene oxide during cycling.

The aforementioned superior electrochemical performance of the 3DGS electrode unambiguously demonstrates that the unique design of sulfur nanoparticles anchored on the 3D sponge is of great advantage. The improved cyclability and rate performance is mainly attributed to the following factors: (1) the pores of 3DGS (Fig. 2a and f) could serve as electrolyte reservoirs, facilitating the penetration of the electrolyte and allowing a high flux of Li⁺ to pass through, as well as improving the absorption ability of the electrode toward the soluble polysulfide ions due to their strong electrolyte absorbability (details of the calculation of electrolyte uptake ability are shown in the ESI†).⁴¹ The pores could also provide enough voids to accommodate volume variation during cycling. (2) The flexibility and robustness of the 3DGS electrode (Fig. 1e and Fig. S9 of ESI†) is able to alleviate the stress arising from the transformation between sulfur and its reduction products, maintaining the integrity of the electrodes during long-term cycling. (3) The 3DGS electrode maintains an interconnected structure without any binder, thus providing a continuous pathway for electron transport, as shown in Fig. 4e. Besides, the residual oxygen-containing functional groups could have strong interactions with sulfur and polysulfide ions.^{41,47} Therefore, the re-deposited sulfur and Li₂S could be well distributed on the sponge, avoiding bulk aggregation and irreversible active mass loss (Fig. S9 of ESI†). (4) The nano-sized sulfur particles could shorten the Li⁺ transport path length⁷ and ultimately enhance the reaction kinetics.^{22,59}

Conclusions

In this work, an optimized approach to fabricate a robust flexible 3D graphene sponge composited with sulfur nanoparticles is reported. This approach is facile, environmentally friendly, and can be easily scaled up. These merits are significant for industrialization. The well-architected 3DGS exhibits excellent continuous conductivity, superior structural integrity and flexibility, which are favourable characteristics to allow use as a cathode without any binder and conductivity additive. When tested at a high rate of 1.5 A g⁻¹, the 3DGS electrode maintains a high reversible capacity of 580 mA h g⁻¹ over 500 cycles, corresponding to a high capacity retention of 78.4% and to a low fading rate of 0.043% per cycle, which is much better than the GS cathode. This flexible 3D structure design is promising to promote sulfur mass loading over the whole electrode and for the material to be applied in flexible Li-S batteries. Moreover, such a facile and environmentally-benign strategy for constructing a flexible 3D structure may be extended to the design of other energy storage materials.

Acknowledgements

This work was supported by the National Basic Research Program of China (2013CB934103), the Program for Professor

of Special Appointment (Eastern Scholar) at Shanghai Institutions of Higher Learning (TP2015002), the National Natural Science Foundation of China (51521001, 51272197), the National Natural Science Fund for Distinguished Young Scholars (51425204), the Hubei Provincial Natural Science Fund for Distinguished Young Scholars (2014CFA035), and the Fundamental Research Funds for the Central Universities (WUT: 2015-PY-2).

Notes and references

- M. Armand and J. M. Tarascon, *Nature*, 2008, **451**, 652–657.
- A. Manthiram, Y. Fu, S. H. Chung, C. Zu and Y. S. Su, *Chem. Rev.*, 2014, **114**, 11751–11787.
- L. Mai, X. Tian, X. Xu, L. Chang and L. Xu, *Chem. Rev.*, 2014, **114**, 11828–11862.
- X. Ji, K. T. Lee and L. F. Nazar, *Nat. Mater.*, 2009, **8**, 500–506.
- J. Fu, J. Zhang, X. Song, H. Zarrin, X. Tian, J. Qiao, L. Rasen, K. Li and Z. Chen, *Energy Environ. Sci.*, 2016, **9**, 663–670.
- C. Zu and A. Manthiram, *Adv. Energy Mater.*, 2013, **3**, 1008–1012.
- Y. Qiu, W. Li, W. Zhao, G. Li, Y. Hou, M. Liu, L. Zhou, F. Ye, H. Li, Z. Wei, S. Yang, W. Duan, Y. Ye, J. Guo and Y. Zhang, *Nano Lett.*, 2014, **14**, 4821–4827.
- C. Wang, X. Wang, Y. Wang, J. Chen, H. Zhou and Y. Huang, *Nano Energy*, 2015, **11**, 678–686.
- X. Li, Y. Cao, W. Qi, L. V. Saraf, J. Xiao, Z. Nie, J. Mietek, J.-G. Zhang, B. Schwenzer and J. Liu, *J. Mater. Chem.*, 2011, **21**, 16603–16610.
- G. Zhou, E. Paek, G. S. Hwang and A. Manthiram, *Nat. Commun.*, 2015, **6**, 7760.
- B. Papandrea, X. Xu, Y. Xu, C.-Y. Chen, Z. Lin, G. Wang, Y. Luo, M. Liu, Y. Huang, L. Mai and X. Duan, *Nano Res.*, 2016, **9**, 240–248.
- Y. Cao, X. Li, I. A. Aksay, J. Lemmon, Z. Nie, Z. Yang and J. Liu, *Phys. Chem. Chem. Phys.*, 2011, **13**, 7660–7665.
- Q. Zhang, Y. Wang, Z. W. Seh, Z. Fu, R. Zhang and Y. Cui, *Nano Lett.*, 2015, **15**, 3780–3786.
- Z. Wang, Y. Dong, H. Li, Z. Zhao, H. Bin Wu, C. Hao, S. Liu, J. Qiu and X. W. Lou, *Nat. Commun.*, 2014, **5**, 5002.
- J. Zheng, M. Gu, H. Chen, P. Meduri, M. H. Engelhard, J.-G. Zhang, J. Liu and J. Xiao, *J. Mater. Chem. A*, 2013, **1**, 8464–8470.
- M. L. Gordin, F. Dai, S. Chen, T. Xu, J. Song, D. Tang, N. Azimi, Z. Zhang and D. Wang, *ACS Appl. Mater. Interfaces*, 2014, **6**, 8006–8010.
- M. Cuisinier, C. Hart, M. Balasubramanian, A. Garsuch and L. F. Nazar, *Adv. Energy Mater.*, 2015, **5**, 1401801.
- Q. Wang, J. Jin, X. Wu, G. Ma, J. Yang and Z. Wen, *Phys. Chem. Chem. Phys.*, 2014, **16**, 21225–21229.
- A. G. Simmonds, J. J. Griebel, J. Park, K. R. Kim, W. J. Chung, V. P. Oleshko, J. Kim, E. T. Kim, R. S. Glass, C. L. Soles, Y.-E. Sung, K. Char and J. Pyun, *ACS Macro Lett.*, 2014, **3**, 229–232.
- L. Xiao, Y. Cao, J. Xiao, B. Schwenzer, M. H. Engelhard, L. V. Saraf, Z. Nie, G. J. Exarhos and J. Liu, *J. Mater. Chem. A*, 2013, **1**, 9517–9526.
- Z. Sun, M. Xiao, S. Wang, D. Han, S. Song, G. Chen and Y. Meng, *J. Mater. Chem. A*, 2014, **2**, 9280–9286.
- G. Zhou, L.-C. Yin, D.-W. Wang, L. Li, S. Pei, I. R. Gentle, F. Li and H.-M. Cheng, *ACS Nano*, 2013, **7**, 5367–5375.
- Z. Wei Seh, W. Li, J. J. Cha, G. Zheng, Y. Yang, M. T. McDowell, P.-C. Hsu and Y. Cui, *Nat. Commun.*, 2013, **4**, 1331.
- C. Wan, W. Wu, C. Wu, J. Xu and L. Guan, *RSC Adv.*, 2015, **5**, 5102–5106.
- M. Yu, A. Wang, F. Tian, H. Song, Y. Wang, C. Li, J.-D. Hong and G. Shi, *Nanoscale*, 2015, **7**, 5292–5298.
- G. Zhou, Y. Zhao, C. Zu and A. Manthiram, *Nano Energy*, 2015, **12**, 240–249.
- L. Chai, J. Wang, H. Wang, L. Zhang, W. Yu and L. Mai, *Nano Energy*, 2015, **17**, 224–232.
- Z. Xiao, Z. Yang, L. Wang, H. Nie, M. E. Zhong, Q. Lai, X. Xu, L. Zhang and S. Huang, *Adv. Mater.*, 2015, **27**, 2891–2898.
- C.-Y. Fan, H.-H. Li, L.-L. Zhang, H.-Z. Sun, X.-L. Wu, H.-M. Xie and J.-P. Zhang, *Phys. Chem. Chem. Phys.*, 2015, **17**, 23481–23488.
- Y. Huang, M. Zheng, Z. Lin, B. Zhao, S. Zhang, J. Yang, C. Zhu, H. Zhang, D. Sun and Y. Shi, *J. Mater. Chem. A*, 2015, **3**, 10910–10918.
- L. Ji, M. Rao, S. Aloni, L. Wang, E. J. Cairns and Y. Zhang, *Energy Environ. Sci.*, 2011, **4**, 5053–5059.
- L. Zeng, F. Pan, W. Li, Y. Jiang, X. Zhong and Y. Yu, *Nanoscale*, 2014, **6**, 9579–9587.
- Y. Zhou, C. Zhou, Q. Li, C. Yan, B. Han, K. Xia, Q. Gao and J. Wu, *Adv. Mater.*, 2015, **27**, 3774–3781.
- F. Jin, S. Xiao, L. Lu and Y. Wang, *Nano Lett.*, 2016, **16**, 440–447.
- M. Rao, W. Li and E. J. Cairns, *Electrochem. Commun.*, 2012, **17**, 1–5.
- H. B. Wu, S. Wei, L. Zhang, R. Xu, H. H. Hng and X. W. Lou, *Chem. – Eur. J.*, 2013, **19**, 10804–10808.
- W. Zhou, C. Wang, Q. Zhang, H. D. Abruña, Y. He, J. Wang, S. X. Mao and X. Xiao, *Adv. Energy Mater.*, 2015, **5**, 1401752.
- S. Evers and L. F. Nazar, *Chem. Commun.*, 2012, **48**, 1233–1235.
- Z. Peng, W. Fang, H. Zhao, J. Fang, H. Cheng, T. N. L. Doan, J. Xu and P. Chen, *J. Power Sources*, 2015, **282**, 70–78.
- L. Ji, M. Rao, H. Zheng, L. Zhang, Y. Li, W. Duan, J. Guo, E. J. Cairns and Y. Zhang, *J. Am. Chem. Soc.*, 2011, **133**, 18522–18525.
- G. Hu, C. Xu, Z. Sun, S. Wang, H. M. Cheng, F. Li and W. Ren, *Adv. Mater.*, 2016, **28**, 1603–1609.
- Y. Xie, Z. Meng, T. Cai and W. Q. Han, *ACS Appl. Mater. Interfaces*, 2015, **7**, 25202–25210.
- B. He, W. C. Li, C. Yang, S. Q. Wang and A. H. Lu, *ACS Nano*, 2016, **10**, 1633–1639.
- J.-L. Shi, H.-J. Peng, L. Zhu, W. Zhu and Q. Zhang, *Carbon*, 2015, **92**, 96–105.
- J. He, Y. Chen, P. Li, F. Fu, Z. Wang and W. Zhang, *J. Mater. Chem. A*, 2015, **3**, 18605–18610.
- Y. Jiang, M. Lu, X. Ling, Z. Jiao, L. Chen, L. Chen, P. Hu and B. Zhao, *J. Alloys Compd.*, 2015, **645**, 509–516.
- C. Wang, K. Su, W. Wan, H. Guo, H. Zhou, J. Chen, X. Zhang and Y. Huang, *J. Mater. Chem. A*, 2014, **2**, 5018–5023.

- 48 S. Niu, W. Lv, C. Zhang, Y. Shi, J. Zhao, B. Li, Q.-H. Yang and F. Kang, *J. Power Sources*, 2015, **295**, 182–189.
- 49 B. Li, S. Li, J. Liu and J. Xu, *RSC Adv.*, 2015, **5**, 40310–40315.
- 50 H. Li, X. Yang, X. Wang, M. Liu, F. Ye, J. Wang, Y. Qiu, W. Li and Y. Zhang, *Nano Energy*, 2015, **12**, 468–475.
- 51 L. Sun, D. Wang, Y. Luo, K. Wang, W. Kong, Y. Wu, L. Zhang, K. Jiang, Q. Li, Y. Zhang, J. Wang and S. Fan, *ACS Nano*, 2016, **10**, 1300–1308.
- 52 Y. Xu, C.-Y. Chen, Z. Zhao, Z. Lin, C. Lee, X. Xu, C. Wang, Y. Huang, M. I. Shakir and X. Duan, *Nano Lett.*, 2015, **15**, 4605–4610.
- 53 G. Li, J. Sun, W. Hou, S. Jiang, Y. Huang and J. Geng, *Nat. Commun.*, 2016, **7**, 10601.
- 54 L. Zhang, L. Ji, P.-A. Glans, Y. Zhang, J. Zhu and J. Guo, *Phys. Chem. Chem. Phys.*, 2012, **14**, 13670–13675.
- 55 Y. Xu, Z. Lin, X. Zhong, X. Huang, N. O. Weiss, Y. Huang and X. Duan, *Nat. Commun.*, 2014, **5**, 4554.
- 56 A. Yamada, S. C. Chung and K. Hinokuma, *J. Electrochem. Soc.*, 2001, **148**, A224–A229.
- 57 M.-Q. Zhao, Q. Zhang, J.-Q. Huang, G.-L. Tian, J.-Q. Nie, H.-J. Peng and F. Wei, *Nat. Commun.*, 2014, **5**, 3410.
- 58 R. Fang, S. Zhao, P. Hou, M. Cheng, S. Wang, H. M. Cheng, C. Liu and F. Li, *Adv. Mater.*, 2016, **28**, 3374–3382.
- 59 Q. Zhao, X. Hu, K. Zhang, N. Zhang, Y. Hu and J. Chen, *Nano Lett.*, 2015, **15**, 721–726.